PREDICTIVE COMPOSITE GUIDING VECTOR FIELD FOR 3D MANIPULATOR PATH FOLLOWING WITH FULL-LINK OBSTACLE AVOIDANCE

Anonymous authors
Paper under double-blind review

ABSTRACT

Safe manipulator path following requires convergence of the end effector to a desired path while maintaining clearance for all modeled links, particularly near moving obstacles and narrow passages. We propose a predictive composite guiding vector field for 3D path following with full-link collision avoidance. An implicit-surface guiding field provides nominal motion, while capsule models and predicted capsule-aware obstacle levels account for link thickness and anticipate collisions. Moving-boundary compensation handles dynamic obstacles. A rank-discounted global index preserves dominant-threat information for event observation and rejoining, while simultaneous link corrections are reconciled by weighted damped least-squares. After threat release, event-driven safety rejoining (EDSR) modulates convergence and tangential gains under safety gating, and bounded joint commands are obtained by damped inverse kinematics. MATLAB experiments with static, moving, and narrow-frame obstacles show predictive activation and positive capsule-surface clearance; CoppeliaSim co-simulation and a UR7e experiment further illustrate the feasibility of obstacle avoidance and path recovery on simulated and physical platforms.

1 INTRODUCTION

Path following is central to manipulator tasks such as inspection, welding, surface processing, and autonomous manipulation (Loukas et al., 2023; Wen & Pagilla, 2021; Somasundar & Yedukondalu, 2024). Unlike trajectory tracking, it regulates the end effector toward a geometric path without a fixed time parameterization (Cenerini et al., 2023), allowing progression to adapt online when an unexpected obstacle requires a temporary detour. Safe execution, however, requires more than end-effector accuracy: the articulated body must avoid collisions while preserving feasible joint motion. Combining 3D path following with full-link avoidance is therefore essential in cluttered and dynamic environments.

Static obstacles require collision-free detours and recovery, moving obstacles require anticipation of future relative motion, and narrow-frame traversal can activate multiple intermediate-link threats even when the end effector remains clear. These cases require predictive guidance that accounts for link thickness and concurrent link threats (Tamizi et al., 2023; Liu et al., 2024).

Guiding vector fields (GVFs) provide continuous feedback directions toward and along a geometric path (Zhou et al., 2025). Extending this principle to articulated manipulators, however, requires finite-link geometry and the reconciliation of simultaneous corrections associated with different link Jacobians.

Dynamic environments add prediction and recovery requirements. A response based only on current separation can be activated too late, whereas manipulator path following additionally requires moving-boundary information to be coupled with link-level geometry and joint-space control. Avoidance also displaces the end effector from the path. Nominal recovery can be slow, while aggressive or fixed-window recovery may conflict with renewed threats or cause abrupt commands. We therefore use avoidance-event memory and safety gating to accelerate rejoining only after threat release. The overall framework of the proposed method is illustrated in Fig. 1.

Reviewers: please read the Reviewer Guidelines (iclr.cc/Conferences/2027/ReviewerGuidelines) and the AI Policy for Reviewers (iclr.cc/Conferences/2027/AIPolicyForReviewers). If you used AI to expand, edit, or polish your review, please provide the input text to the LLM. Better still, consider skipping the LLM and submitting your original text: we, and the authors, are much more interested in your unedited thoughts than in what an LLM has to say. AI-assisted or not, you are putting your name and reputation behind your review: LLM-generated falsehoods, hallucinations or misrepresentations are subject to disciplinary action, which may include desk-rejecting all papers you have authored.

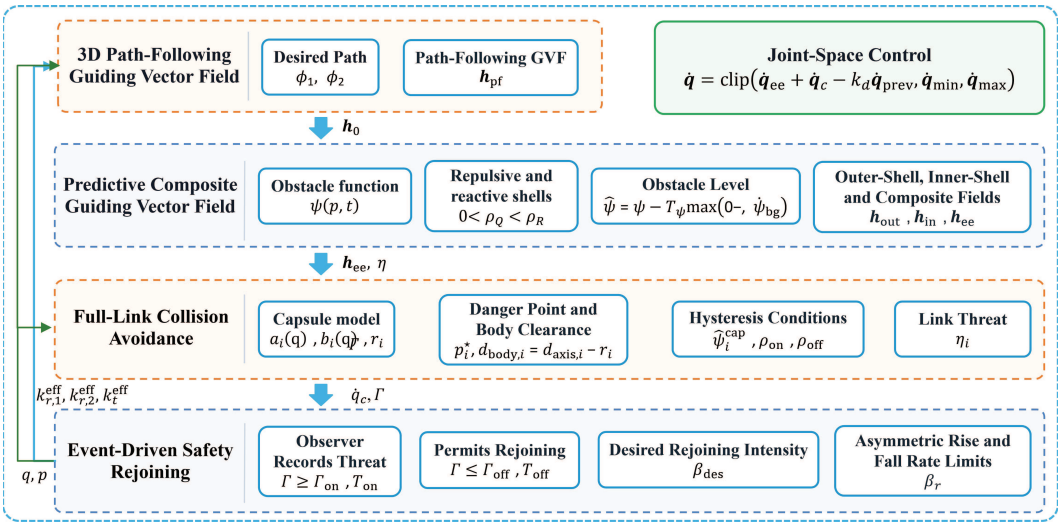

Figure 1: Overview of the proposed predictive composite guiding vector field framework.

The main contributions of this work are summarized as follows:

- We integrate 3D path following, approach-only obstacle prediction, and moving-boundary compensation in a predictive composite GVF.
- We develop capsule-based full-link avoidance: a rank-discounted index summarizes global threat, while weighted joint-space correction handles simultaneously active links.
- We introduce event-driven safety rejoining (EDSR) with event memory and safety gating, and evaluate the complete framework in MATLAB, CoppeliaSim, and on a UR7e manipulator.

2 Related Work

Guiding Vector Fields for Path Following and Collision Avoidance. GVFs drive a system toward and along a path represented by one or more smooth implicit zero-level sets (Kapitanyuk et al., 2017; Yao et al., 2021). This principle has been extended to three-dimensional and partially occluded paths (Yao, 2023b;a). For obstacle avoidance, Yao et al. (2019) combine path-following and avoidance fields through bump functions defined over reactive and repulsive regions. This construction provides continuous local guidance, but its planar point-robot formulation with stationary obstacles does not represent finite link thickness or protect intermediate manipulator links. More recent dynamical-system approaches reshape nominal motion through rotational or diffeomorphic transformations to handle complex obstacle geometries (Huber et al., 2023; Simmoteit et al., 2025).

Full-Link Collision Avoidance in Dynamic Environments. Recent manipulator collision-avoidance methods include constraint enforcement, CBF-guided MPC, uncertainty-aware safe planning, and high-performance whole-body control (Koutras et al., 2023; Liu et al., 2025; Michaux et al., 2025; Eckhoff et al., 2023). For online collision evaluation, differentiable robot-geometry and configuration-space distance-field representations provide smooth distance queries for collision-aware optimization (Li et al., 2024b;a). Multi-objective policy composition and GPU-parallel optimization have also been investigated to reconcile competing motion objectives and accelerate collision-free motion generation (Urain et al., 2023; Sundaralingam et al., 2023). Dynamic avoidance additionally requires accounting for obstacle motion and future relative motion (Krämer et al., 2020; Li et al., 2021; Zhu et al., 2023; Chen et al., 2026). Braquet & Bakolas (2022) construct a vector field for a point agent navigating around moving ellipses, but consider goal reaching rather than articulated manipulator path following. Moreover, conventional reactive blending generally restores nominal guidance after clearance without explicitly regulating the post-avoidance recovery process. The present framework instead combines predictive activation, capsule-based multi-link correction, a global threat index, and EDSR.

3 METHOD

3.1 PROBLEM FORMULATION AND 3D PATH-FOLLOWING GUIDING VECTOR FIELD

Consider a six-degree-of-freedom manipulator with joint configuration $\boldsymbol{q} \in \mathbb{R}^6$, end-effector position $\boldsymbol{p} = f(\boldsymbol{q}) \in \mathbb{R}^3$, where $f(\cdot)$ denotes forward-kinematics mapping and translational Jacobian $\boldsymbol{J}_v(\boldsymbol{q}) \in \mathbb{R}^{3\times 6}$, such that $\dot{\boldsymbol{p}} = \boldsymbol{J}_v(\boldsymbol{q})\dot{\boldsymbol{q}}$. The objective is to follow a prescribed spatial path while preventing the end effector and all modeled links from colliding with static or moving obstacles.

The desired path is represented as the intersection of two smooth implicit surfaces. Define $\boldsymbol{\phi}(\boldsymbol{p}) = [\phi_1(\boldsymbol{p}), \phi_2(\boldsymbol{p})]^\mathsf{T}$. The path and its associated error are

$$\mathcal{P} = \left\{ \boldsymbol{p} \in \mathbb{R}^3 \mid \boldsymbol{\phi}(\boldsymbol{p}) = \boldsymbol{0} \right\}, \qquad e_{\text{path}} = \|\boldsymbol{\phi}(\boldsymbol{p})\|_2. \tag{1}$$

Let $\boldsymbol{n}_i = \nabla\phi_i/\|\nabla\phi_i\|_2$ and $\boldsymbol{\tau} = (\boldsymbol{n}_2 \times \boldsymbol{n}_1)/\|\boldsymbol{n}_2 \times \boldsymbol{n}_1\|_2$ denote the normalized surface normals and path tangent, respectively. The nominal path-following guiding vector field is

$$\boldsymbol{h}_{\text{pf}} = -k_{r,1}^{\text{eff}}\phi_1\boldsymbol{n}_1 - k_{r,2}^{\text{eff}}\phi_2\boldsymbol{n}_2 + k_t^{\text{eff}}\boldsymbol{\tau}. \tag{2}$$

The first two terms in equation (2) drive the end effector toward the path, whereas the last term generates tangential motion along it. To reduce excessive tangential motion far from the path, its nominal gain is adjusted as $k_t^{\text{base}} = k_{t,\min} + (k_t - k_{t,\min})\delta_r/(e_{\text{path}} + \delta_r)$, where k_t and $k_{t,\min}$ are the nominal and minimum tangential gains, respectively, and $\delta_r > 0$ sets the path-error transition scale. The effective gains are further modulated by the rejoining mechanism introduced in Section 3.3.

3.2 PREDICTIVE COMPOSITE GUIDING VECTOR FIELD FOR FULL-LINK COLLISION AVOIDANCE

An obstacle is represented by a differentiable implicit function $\psi(\boldsymbol{p}, t)$, where $\psi < 0$, $\psi = 0$, and $\psi > 0$ correspond to the interior, boundary, and exterior of the obstacle, respectively. Two levels $0 < \rho_Q < \rho_R$ define the repulsive and reactive shells. Let $\text{sat}_{[0,1]}(s) = \min\{1, \max\{0, s\}\}$. Let $\boldsymbol{v}_{\text{bg}}$ denote the background Cartesian velocity of the point at which ψ is evaluated. For end-effector prediction, $\boldsymbol{v}_{\text{bg}} = \boldsymbol{h}_0$, where $\boldsymbol{h}_0 = \boldsymbol{h}_{\text{pf}}$ is the current path-following field. To activate avoidance before an imminent encounter, the obstacle level is predicted over a horizon T_ψ:

$$\begin{aligned} \dot{\psi}_{\text{bg}} &= \nabla_{\boldsymbol{p}}\psi^\mathsf{T}\boldsymbol{v}_{\text{bg}} + \frac{\partial\psi}{\partial t}, \\ \widehat{\psi} &= \psi - T_\psi \max(0, -\dot{\psi}_{\text{bg}}), \\ \eta &= 1 - \text{sat}_{[0,1]}\left(\frac{\widehat{\psi} - \rho_Q}{\rho_R - \rho_Q}\right). \end{aligned} \tag{3}$$

Here, $\dot{\psi}_{\text{bg}}$ denotes the obstacle-level variation rate, $\widehat{\psi}$ is the predicted obstacle level, and η denotes the end-effector threat.

The approach-only prediction in equation (3) reduces $\widehat{\psi}$ when the robot and obstacle approach each other but does not enlarge it when they move apart. Define the obstacle normal $\boldsymbol{n} = \nabla_{\boldsymbol{p}}\psi/\|\nabla_{\boldsymbol{p}}\psi\|_2$ and tangent-plane projection $\boldsymbol{\Pi} = \boldsymbol{I}_3 - \boldsymbol{n}\boldsymbol{n}^\mathsf{T}$, where $\boldsymbol{I}_3$ denotes the 3×3 identity matrix. The outward boundary velocity is $v_n^+ = \max(0, -(\partial\psi/\partial t)/\|\nabla_{\boldsymbol{p}}\psi\|_2)$.

Using the current path-following field $\boldsymbol{h}_0$ defined above, let $\boldsymbol{v}_{\text{obs}}$ denote the translational velocity of the obstacle center. The obstacle-velocity feedforward term is defined as $\boldsymbol{v}_{\text{ff}} = k_{\text{ff}}\eta\boldsymbol{v}_{\text{obs}}$, where $k_{\text{ff}} \geq 0$ is the feedforward gain. The avoidance field is constructed in the relative obstacle-velocity frame using $\boldsymbol{h}_{0,\text{rel}} = \boldsymbol{h}_0 - \boldsymbol{v}_{\text{ff}}$. For a static obstacle, $\boldsymbol{v}_{\text{obs}} = \boldsymbol{0}$ and thus $\boldsymbol{h}_{0,\text{rel}} = \boldsymbol{h}_0$.

Let $\boldsymbol{t}_o = \boldsymbol{\Pi}\boldsymbol{h}_{0,\text{rel}}/\|\boldsymbol{\Pi}\boldsymbol{h}_{0,\text{rel}}\|_2$ denote the normalized projection of $\boldsymbol{h}_{0,\text{rel}}$ onto the local obstacle tangent plane, and let $\boldsymbol{q}_o = \mathcal{R}(r_o\boldsymbol{n}, \alpha_{\text{in}})\boldsymbol{t}_o$ denote the corresponding inner-shell circulation direction, where $r_o \in \{-1, +1\}$ denotes the circulation sign and $\mathcal{R}(\cdot,\cdot)$ is the Rodrigues rotation operator.

Upon the first entry into the reactive shell, r_o is selected as the sign whose candidate inner-shell circulation direction has the larger projection onto the path tangent $\boldsymbol{\tau}$. If insufficient tangential progress and path-error reduction, together with either a small avoidance-field magnitude or entry into the inner shell, persist for a prescribed dwell time, the circulation sign is reversed as $r_o \leftarrow -r_o$. The outer-shell, inner-shell, and composite fields are

$$\begin{aligned} \boldsymbol{h}_{\mathrm{out}} &= \mathcal{R}\left(r_o \boldsymbol{n}, \eta \alpha_{\mathrm{out}}\right)\left[\boldsymbol{h}_{0,\mathrm{rel}} + \eta\left(k_{o,\mathrm{out}}\|\boldsymbol{h}_{0,\mathrm{rel}}\|_2 + v_{\mathrm{comp}}\right)\boldsymbol{n}\right], \\ \boldsymbol{h}_{\mathrm{in}} &= \|\boldsymbol{h}_{0,\mathrm{rel}}\|_2 \boldsymbol{q}_o + \left(k_{o,\mathrm{in}}\eta\|\boldsymbol{h}_{0,\mathrm{rel}}\|_2 + v_n^+\right)\boldsymbol{n}, \\ \boldsymbol{h}_{\mathrm{ee}} &= \begin{cases} b(1-\eta)\boldsymbol{h}_{\mathrm{out}} + [1 - b(1-\eta)]\boldsymbol{h}_{\mathrm{in}} + \boldsymbol{v}_{\mathrm{ff}}, & \widehat{\psi} < \rho_R, \\ \boldsymbol{h}_0, & \widehat{\psi} \geq \rho_R. \end{cases} \end{aligned} \tag{4}$$

where $b(s) = 3s^2 - 2s^3$ is the smooth blending function and $v_{\mathrm{comp}} = \max(0, v_n^+ - \boldsymbol{n}^{\mathsf{T}}\boldsymbol{h}_{0,\mathrm{rel}})$ is the moving-boundary compensation term. Here, α_{out} and α_{in} are the outer- and inner-shell rotation angles, while $k_{o,\mathrm{out}}$ and $k_{o,\mathrm{in}}$ are the corresponding outward gains.

To account for the complete manipulator geometry, link i is modeled as a capsule defined by centerline endpoints $\boldsymbol{a}_i(\boldsymbol{q})$ and $\boldsymbol{b}_i(\boldsymbol{q})$ and radius r_i. Its danger point is selected along the centerline, and the body clearance is evaluated by

$$\begin{aligned} s_i^\star &= \operatorname*{arg\,min}_{s\in[0,1]} \psi(\boldsymbol{a}_i + s(\boldsymbol{b}_i - \boldsymbol{a}_i), t), \\ \boldsymbol{p}_i^\star &= \boldsymbol{a}_i + s_i^\star(\boldsymbol{b}_i - \boldsymbol{a}_i), \\ d_{\mathrm{body},i} &= d_{\mathrm{axis},i} - r_i. \end{aligned} \tag{5}$$

Here, $s_i^\star$ is the centerline parameter that selects the danger point $\boldsymbol{p}_i^\star$, and $d_{\mathrm{axis},i}$ denotes the signed Euclidean distance from $\boldsymbol{p}_i^\star$ to the obstacle surface.

For an obstacle gauge satisfying $\psi = g^2 - 1$, link thickness is incorporated through $g_i^{\mathrm{cap}} = \max(0, g - r_i/\ell_{\min})$ and $\psi_i^{\mathrm{cap}} = (g_i^{\mathrm{cap}})^2 - 1$, where g_i^{cap} denotes the capsule-adjusted obstacle gauge, ψ_i^{cap} is the corresponding capsule-aware obstacle level, $g = \sqrt{\max(1+\psi, 0)}$, and $\ell_{\min}$ is the minimum characteristic obstacle scale. For frame obstacles, the bar radius is directly enlarged by r_i.

For the danger point $\boldsymbol{p}_i^\star$, the background Cartesian velocity in equation (3) is set to $\boldsymbol{v}_{\mathrm{bg},i} = \boldsymbol{J}_i\dot{\boldsymbol{q}}_{\mathrm{ee}}$, where $\boldsymbol{J}_i$ is the translational Jacobian evaluated at the current danger point and $\dot{\boldsymbol{q}}_{\mathrm{ee}}$ is the end-effector task command defined in equation (10). Applying equation (3) with $\boldsymbol{v}_{\mathrm{bg}} = \boldsymbol{v}_{\mathrm{bg},i}$ gives the predicted capsule-aware level $\widehat{\psi}_i^{\mathrm{cap}}$. Let $\rho_{\mathrm{on}} > \rho_Q$ denote the link-level activation threshold for the predicted capsule-aware level, which is distinct from the global event threshold Γ_{on} introduced in Section 3.3. The corresponding link threat and the rank-discounted overall threat are

$$\begin{aligned} \eta_i &= 1 - \mathrm{sat}_{[0,1]}\left(\frac{\widehat{\psi}_i^{\mathrm{cap}} - \rho_Q}{\rho_{\mathrm{on}} - \rho_Q}\right), \\ \Gamma &= 1 - \prod_{j=1}^{L+1}\left(1 - \eta_{(j)}\right)^{q_\Gamma^{j-1}}, \qquad 0 < q_\Gamma \leq 1, \end{aligned} \tag{6}$$

where L is the number of capsule-modeled links and $\eta_{(1)} \geq \cdots \geq \eta_{(L+1)}$ are the sorted $L+1$ threats, comprising one end-effector threat and L link-level threats. Here, q_Γ denotes the rank-discount parameter. As q_Γ approaches zero, equation (6) approaches the maximum threat, whereas intermediate values preserve contributions from simultaneous threats while emphasizing the most critical one.

For link correction, the link-correction threat weight η_i^{ctrl} is defined as $\eta_i^{\mathrm{ctrl}} = \eta_i^{\mathrm{cur}} + k_{\mathrm{pre}}\max(0, \eta_i - \eta_i^{\mathrm{cur}})$, where η_i^{cur} denotes the current link threat obtained from the definition of η_i in equation (6) by replacing $\widehat{\psi}_i^{\mathrm{cap}}$ with ψ_i^{cap}, and $k_{\mathrm{pre}} \in [0, 1]$ is the prediction-preview gain.

For each active link, all obstacle quantities are evaluated at the danger point $\boldsymbol{p}_i^\star$. Let $\boldsymbol{t}_i = \boldsymbol{\Pi}\boldsymbol{v}_{\mathrm{bg},i}/\|\boldsymbol{\Pi}\boldsymbol{v}_{\mathrm{bg},i}\|_2$ denote the normalized projection of the background velocity onto the local obstacle tangent plane. When this projection is degenerate, the projected path tangent $\boldsymbol{\Pi}\boldsymbol{\tau}$ is used, followed by an arbitrary tangent direction if necessary.

The circulation sign is selected as $r_{\mathrm{cir},i} = \arg\max_{r\in\{-1,+1\}} \boldsymbol{\tau}^\mathsf{T}\mathcal{R}(r\boldsymbol{n}, \alpha_{\max})\boldsymbol{t}_i$, with the previous sign retained in the case of a tie. Define the link-specific circulation angle $\alpha_i = \eta_i^{\mathrm{ctrl}}\alpha_{\max}$ and the corresponding circulation direction $\boldsymbol{q}_{\mathrm{cir},i} = \mathcal{R}(r_{\mathrm{cir},i}\boldsymbol{n}, \alpha_i)\boldsymbol{t}_i$. The local correction is then $\Delta\boldsymbol{v}_i = \boldsymbol{v}_{\mathrm{push},i} + \boldsymbol{v}_{\mathrm{cir},i}$, where $\boldsymbol{v}_{\mathrm{push},i} = [k_{\mathrm{push}}\eta_i^{\mathrm{ctrl}}\|\boldsymbol{v}_{\mathrm{bg},i}\|_2 + \max(0, v_n^+ - \boldsymbol{n}^\mathsf{T}\boldsymbol{v}_{\mathrm{bg},i})]\boldsymbol{n}$ and $\boldsymbol{v}_{\mathrm{cir},i} = k_{\mathrm{cir}}\eta_i^{\mathrm{ctrl}}\|\boldsymbol{v}_{\mathrm{bg},i}\|_2\boldsymbol{q}_{\mathrm{cir},i}$. Here, $\boldsymbol{v}_{\mathrm{push},i}$ and $\boldsymbol{v}_{\mathrm{cir},i}$ denote the normal-repulsion and tangential-circulation corrections, respectively; $\alpha_{\max}$ is the maximum circulation angle, while k_{push} and k_{cir} scale normal repulsion and tangential circulation, respectively. These corrections are mapped to joint space through

$$\begin{aligned}\dot{\boldsymbol{q}}_c = \arg\min_{\boldsymbol{z}} \quad & \sum_{i\in\mathcal{A}} \omega_i \left\|\boldsymbol{J}_i\boldsymbol{z} - \Delta\boldsymbol{v}_i\right\|_2^2 + \omega_e \left\|\boldsymbol{J}_v\boldsymbol{z}\right\|_2^2 \\ & + \omega_p \left\|\boldsymbol{\tau}^\mathsf{T}\boldsymbol{J}_v\boldsymbol{z}\right\|_2^2 + \lambda_c^2\|\boldsymbol{z}\|_2^2,\end{aligned} \tag{7}$$

Here, $\boldsymbol{z} \in \mathbb{R}^6$ is the optimization variable, $\dot{\boldsymbol{q}}_c$ the weighted link correction, and $\mathcal{A}$ the hysteresis-based active-link set. An inactive link i enters $\mathcal{A}$ when $\widehat{\psi}_i^{\mathrm{cap}} < \rho_{\mathrm{on}}$. Once activated, it remains active while $\widehat{\psi}_i^{\mathrm{cap}} < \rho_{\mathrm{off}}$ and leaves $\mathcal{A}$ when $\widehat{\psi}_i^{\mathrm{cap}} \geq \rho_{\mathrm{off}}$, where $\rho_{\mathrm{off}} > \rho_{\mathrm{on}}$ is the link-level release threshold and is distinct from the global event threshold Γ_{off}.

The link-task weight ω_i and tangential penalty weight ω_p are defined as $\omega_i = \omega_{\max}(\eta_i^{\mathrm{ctrl}})^{p_\omega}$ and $\omega_p = \omega_{p,0}(1-\max_i \eta_i^{\mathrm{ctrl}})^{p_p}$. Here, $\omega_{\max}$ is the maximum link-task weight, p_ω is its threat exponent, ω_e is the end-effector-motion penalty, $\omega_{p,0}$ and p_p set the tangential penalty, and λ_c is the link-correction damping coefficient. Therefore, collision avoidance receives higher priority as the threat increases, while unintended end-effector displacement and loss of tangential progress are suppressed whenever safety permits.

3.3 Event-Driven Safety Rejoining and Joint-Space Control

The overall threat Γ is used by the rejoining event observer, with $\Gamma_{\mathrm{off}} < \Gamma_{\mathrm{on}}$. In the discrete-time implementation, the event observer and rejoining intensity at sample k are evaluated using the previously computed threat Γ_{k-1}; for compactness, the continuous-time notation $\Gamma(t)$ is retained below.

The observer records threat onset only after $\Gamma \geq \Gamma_{\mathrm{on}}$ persists for T_{on}, and permits rejoining only after $\Gamma \leq \Gamma_{\mathrm{off}}$ persists for T_{off}. Rejoining is interrupted immediately if the threat again satisfies $\Gamma \geq \Gamma_{\mathrm{on}}$ and terminates when $\Gamma \leq \Gamma_{\mathrm{off}}$ and $e_{\mathrm{path}} \leq e_{\mathrm{high}}$ hold for N_{done} consecutive samples.

Let χ_r be one in the rejoining state and zero otherwise, and define the smooth-step function $S(x) = 3x^2 - 2x^3$. The threat variation rate is estimated through the causal finite difference $\dot{\Gamma}(t) = [\Gamma(t) - \Gamma(t - T_\Gamma)]/T_\Gamma$, where $T_\Gamma = 0.02$ s is the finite-difference interval. The desired rejoining intensity is

$$\begin{aligned}\beta_{\mathrm{des}} &= \mathrm{sat}_{[0,1]}\left(\chi_r\beta_s\beta_e A_{\mathrm{trend}}A_{\mathrm{done}}\right), \\ \beta_s &= (1-\Gamma)^{p_\Gamma}, \\ \beta_e &= S\left[\mathrm{sat}_{[0,1]}\left(\frac{e_{\mathrm{path}} - e_{\mathrm{low}}}{e_{\mathrm{high}} - e_{\mathrm{low}}}\right)\right], \\ A_{\mathrm{trend}} &= 1 - S\left[\mathrm{sat}_{[0,1]}\left(\frac{\dot{\Gamma} - r_{\mathrm{start}}}{r_{\mathrm{stop}} - r_{\mathrm{start}}}\right)\right].\end{aligned} \tag{8}$$

Here, β_s, β_e, and A_{trend} are the safety, error, and threat-trend factors, respectively; p_Γ controls threat sensitivity, and $e_{\mathrm{low}} < e_{\mathrm{high}}$ are the error-gating thresholds. The parameters $r_{\mathrm{start}} < r_{\mathrm{stop}}$ are the lower and upper thresholds of the threat variation rate. Moreover, $A_{\mathrm{done}} = 1 -$

Table 1: Main controller parameters used in the MATLAB experiments

PARAMETER	VALUE	PARAMETER	VALUE
T	$10\,\mathrm{s}$	Δt	$0.001\,\mathrm{s}$
$k_{r,1},\ k_{r,2}$	$1.40,\ 1.80$	$k_t,\ k_{t,\min}$	$0.22,\ 0.06$
$k_{o,\mathrm{out}},\ k_{o,\mathrm{in}}$	$0.42,\ 0.95$	$\alpha_{\mathrm{out}},\ \alpha_{\mathrm{in}}$	$42^\circ,\ 86^\circ$
$\rho_Q,\ \rho_R$	$0.55,\ 2.40$	T_ψ	$0.10\,\mathrm{s}$
q_Γ	0.35	$\lambda_{\mathrm{ee}},\ \lambda_c$	$2{\times}10^{-3},\ 5{\times}10^{-3}$
$k_{\mathrm{push}},\ k_{\mathrm{cir}}$	$1.15,\ 0.32$	$\alpha_{\max}$	75°
$\dot{q}_{\max}$	$1.30\,\mathrm{rad/s}$	r_i	$0.015\,\mathrm{m}$
$\Gamma_{\mathrm{on}},\ \Gamma_{\mathrm{off}}$	$0.10,\ 0.03$	$e_{\mathrm{low}},\ e_{\mathrm{high}}$	$0.002,\ 0.012\,\mathrm{m}$
$g_{r,\max},\ g_{t,\min}$	$3.0,\ 0.45$	$T_{\mathrm{on}},\ T_{\mathrm{off}}$	$0.05,\ 0.10\,\mathrm{s}$

$S[\mathrm{sat}_{[0,1]}(c_{\mathrm{done}}/N_{\mathrm{done}})]$, where c_{done} is the number of consecutive samples satisfying $\Gamma \le \Gamma_{\mathrm{off}}$ and $e_{\mathrm{path}} \le e_{\mathrm{high}}$. This term attenuates the rejoining action near completion. This term attenuates the rejoining action near completion. The implemented intensity β_r follows β_{des} through asymmetric rise and fall rate limits and is immediately reset to zero when rejoining is inactive or a new threat is detected.

The path-following gains in equation (2) are modulated according to

$$\begin{aligned} k_{r,i}^{\mathrm{eff}} &= [1 + (g_{r,\max} - 1)\beta_r]\, k_{r,i}, \qquad i \in \{1, 2\}, \\ k_t^{\mathrm{eff}} &= [1 - (1 - g_{t,\min})\beta_r]\, k_t^{\mathrm{base}}. \end{aligned} \tag{9}$$

Here, $k_{r,i}$ are the nominal convergence gains, $g_{r,\max}$ is the maximum convergence multiplier, and $g_{t,\min}$ is the minimum tangential multiplier. Thus, rejoining strengthens convergence toward the path while temporarily reducing tangential progression. The nominal field is recovered continuously as β_r approaches zero.

Finally, the joint-space velocity command is given by

$$\begin{aligned} \dot{\boldsymbol{q}}_{\mathrm{ee}} &= \boldsymbol{J}_v^{\mathsf{T}} \left(\boldsymbol{J}_v \boldsymbol{J}_v^{\mathsf{T}} + \lambda_{\mathrm{ee}}^2 \boldsymbol{I}_3 \right)^{-1} \boldsymbol{h}_{\mathrm{ee}}, \\ \dot{\boldsymbol{q}} &= \mathrm{clip}\left(\dot{\boldsymbol{q}}_{\mathrm{ee}} + \dot{\boldsymbol{q}}_c - k_d \dot{\boldsymbol{q}}_{\mathrm{prev}},\ \dot{\boldsymbol{q}}_{\min},\ \dot{\boldsymbol{q}}_{\max} \right). \end{aligned} \tag{10}$$

Here, λ_{ee} is the inverse-kinematics damping coefficient, clip enforces the componentwise bounds $\dot{\boldsymbol{q}}_{\min}$ and $\dot{\boldsymbol{q}}_{\max}$, $\dot{\boldsymbol{q}}_{\mathrm{prev}}$ is the previous command, and $k_d \ge 0$ is the temporal damping gain. This two-stage mapping assigns the predictive composite field to the end-effector task while incorporating simultaneous full-link avoidance requirements through the weighted correction equation 7.

4 Experiments

We evaluate the method through MATLAB simulations, MATLAB–CoppeliaSim co-simulations, and UR7e experiments. Numerical tests cover static, moving, and narrow-frame obstacles and a controlled rejoining ablation. Unless stated otherwise, each within-scenario comparison uses the same path, initial configuration, obstacle, and duration. We report path error, minimum clearance, overall threat, peak joint speed, and, for recovery tests, rejoining time and accumulated error.

4.1 MATLAB Numerical Validation

All MATLAB tests use a six-degree-of-freedom UR5 with capsule-modeled links; Table 1 lists the common settings. The horizontal circle is defined by $\phi_1 = \sqrt{(x - x_c)^2 + (y - y_c)^2} - R$ and $\phi_2 = z - z_c$. Static and moving tests use $(x_c, y_c, z_c) = (0.30, 0.30, 0.43)\,\mathrm{m}$, $R = 0.15\,\mathrm{m}$, and $\boldsymbol{q}_0 = [-2.35, -1.55, 1.55, -1.55, -1.57, 0]^{\mathsf{T}}\,\mathrm{rad}$; the frame test uses $(0.54, 0, 0.43)\,\mathrm{m}$, $R = 0.085\,\mathrm{m}$, and $\boldsymbol{q}_0 = [-3.424, -2.024, 1.903, -1.334, -1.884, 0]^{\mathsf{T}}\,\mathrm{rad}$.

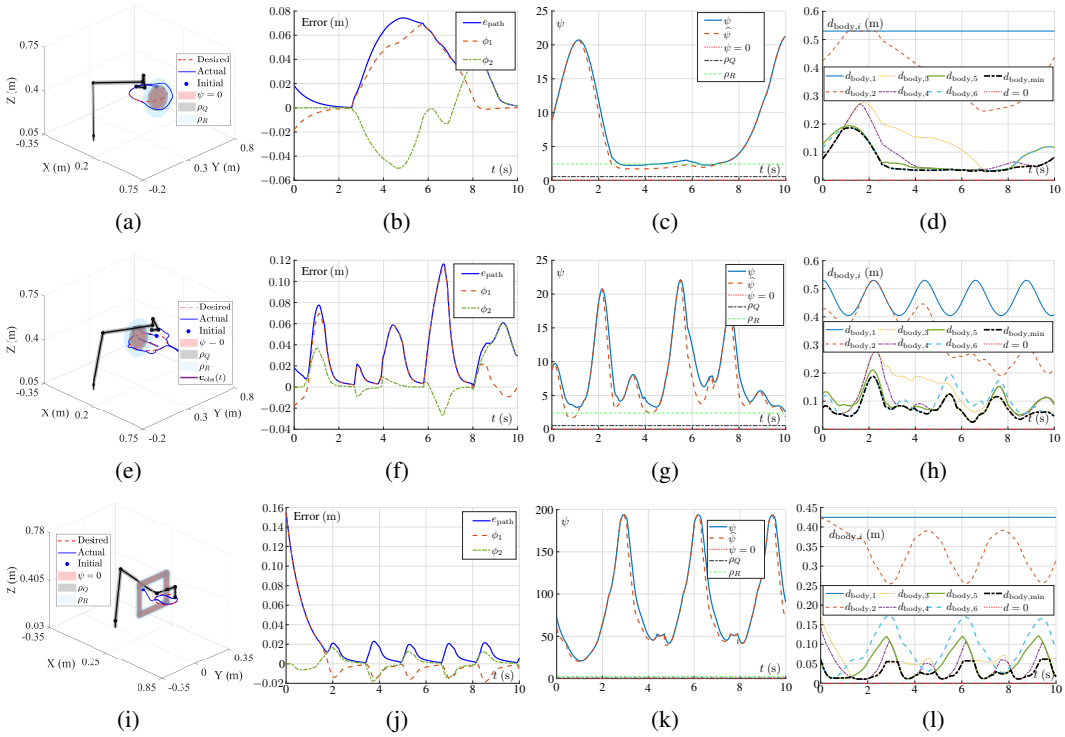

Figure 2: Numerical results for static (top), moving (middle), and narrow-frame (bottom) obstacles. Columns show the 3D path, path errors, obstacle levels, and link capsule-surface clearances.

Static-obstacle avoidance. For the ellipsoid centered at $[0.41, 0.30, 0.43]^\mathsf{T}$ m with semi-axes $[0.055, 0.070, 0.080]^\mathsf{T}$ m, the predicted level enters the reactive shell at 2.556 s, 0.351 s before the current level. As shown in the top row of Fig. 2, the manipulator detours around the obstacle and returns to the path. At most four links activate simultaneously, the minimum capsule-surface clearance remains positive at 0.0320 m, and the path error decreases from its 0.0743 m maximum to 1.45×10^{-3} m at the final time.

Moving-obstacle avoidance. The same ellipsoid moves along x between $[0.41, 0.30, 0.43]^\mathsf{T}$ and $[0.19, 0.30, 0.43]^\mathsf{T}$ m at an average one-way speed of 0.20 m/s and reverses after each 1.10 s traversal. In the middle row of Fig. 2, the current level remains above $\rho_R = 2.40$ (minimum 2.589), whereas the predicted level reaches 1.645, so prediction activates avoidance before the current level alone would do so. Across repeated encounters, at most four links activate, the minimum clearance is 0.0254 m, and the maximum path error is 0.1165 m.

Narrow-frame traversal. The yz-plane frame is centered at $[0.40, 0, 0.43]^\mathsf{T}$ m, with half-spans 0.145 and 0.118 m and bar radius 0.018 m. End-effector levels remain outside the reactive shell, but link threats activate repeatedly during traversal, confirming that end-effector-only monitoring is insufficient. As shown in the bottom row of Fig. 2, at most three links activate and the minimum clearance remains positive at 0.0107 m. The scenario-specific initial configuration produces a 0.1548 m path error, which falls to 6.17×10^{-3} m.

4.2 Ablation Study on the Rejoining Mechanism

We compare four variants under identical avoidance, observer, obstacle, and initial conditions: None sets the rejoining intensity β_r to zero while retaining nominal path following, Fixed window applies a predefined recovery interval, State driven determines recovery from the current state, and EDSR additionally uses threat-trend attenuation, completion fading, and asymmetric rate limits. The rejoining metrics T_{rejoin} and J_{rejoin} are evaluated over the detected post-release rejoining intervals, whereas the minimum clearance and peak joint speed are computed over the entire simulation. Here, the minimum clearance is obtained by taking the minimum over the end-effector point and

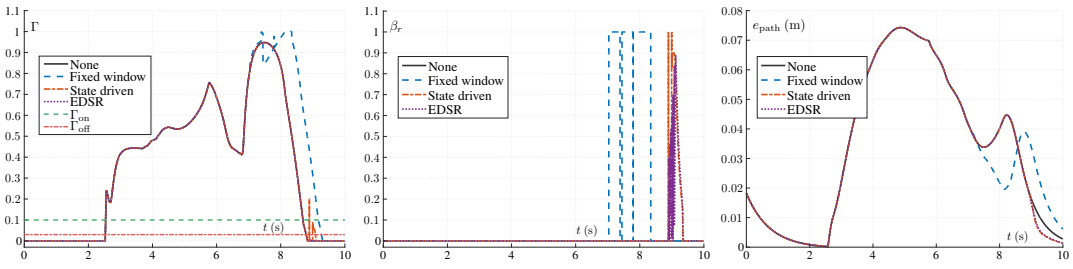

(a) (b) (c)

Figure 3: Four-mode rejoining ablation: predicted threat Γ, rejoining weight β_r, and path error e_{path}. The left panel also shows the activation and release thresholds.

Table 2: Ablation results for the rejoining mechanism

METHOD	T_{rejoin} (s)	J_{rejoin} (m s)	MIN. CLEARANCE (m)	PEAK JOINT SPEED (rad/s)	SUCCESS RATE (%)
None	0.823	8.56×10^{-3}	0.0503	0.487	100
Fixed window	N/C	N/C	0.0509	0.464	0
State driven	0.348	2.91×10^{-3}	0.0487	0.450	50
EDSR	0.471	4.90×10^{-3}	0.0493	0.471	100

all monitored link-capsule surface clearances. Fig. 3 shows the threat, rejoining weight, and path error, while Table 2 summarizes recovery and safety metrics.

Relative to None, EDSR reduces T_{rejoin} from 0.823 to 0.471 s and J_{rejoin} from 8.56×10^{-3} to 4.90×10^{-3} m s (42.8% and 42.7%), while maintaining 0.0493 m minimum clearance and 0.471 rad/s peak joint speed. Fixed window does not complete before the simulation ends. State driven is faster for its successful recovery, but only one of its two detected rejoining events completes, resulting in a 50% success rate. EDSR completes all detected events, achieving a 100% success rate and providing a more consistent balance of recovery speed, clearance, and joint motion.

4.3 MATLAB–CoppeliaSim Co-Simulation

MATLAB–CoppeliaSim co-simulation evaluates the controller with simulator communication, discrete command updates, and a physics-based UR5 model. MATLAB computes the field, link threats, and joint commands online; CoppeliaSim executes the motion and returns robot and obstacle states. The corresponding numerical settings are retained except for the 15 s duration. Fig. 4 shows the resulting path following, full-link avoidance, and rejoining sequence.

4.4 Physical Experiment on the UR7e Manipulator

The method is finally implemented on a physical UR7e to evaluate its feasibility on a real robotic platform. After the obstacle geometry and pose are calibrated in the robot base frame, a host computer computes joint-velocity commands online and transmits them through the robot interface; joint and end-effector states are recorded throughout the experiment. The experiment examines continuous 3D path following, obstacle avoidance by the modeled robot body, and recovery after threat release. Fig. 5 qualitatively illustrates the approach, avoidance, and rejoining phases during physical execution.

5 Conclusion and Limitations

We presented a predictive composite GVF for 3D manipulator path following with capsule-based full-link avoidance, rank-discounted global threat aggregation, and EDSR. Numerical, co-simulation, and physical results demonstrate anticipatory response to static and moving obstacles,

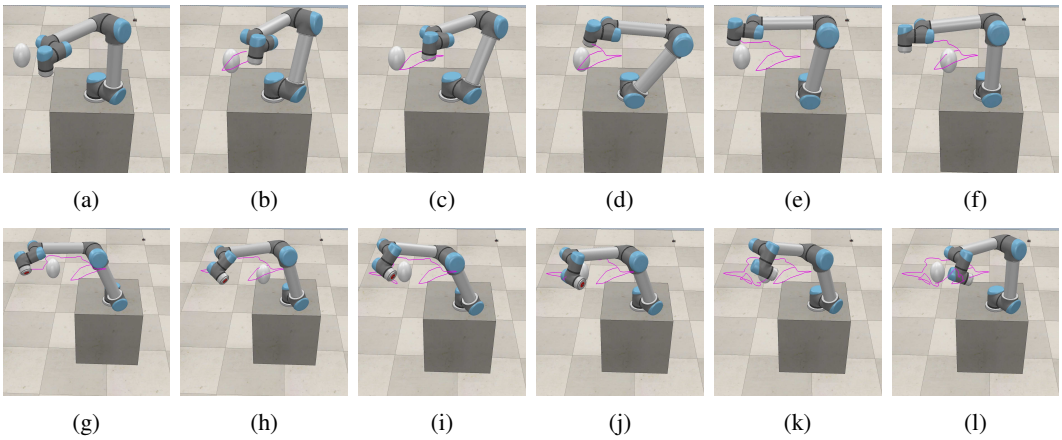

Figure 4: Chronological co-simulation snapshots showing path following, full-link avoidance, and path rejoining.

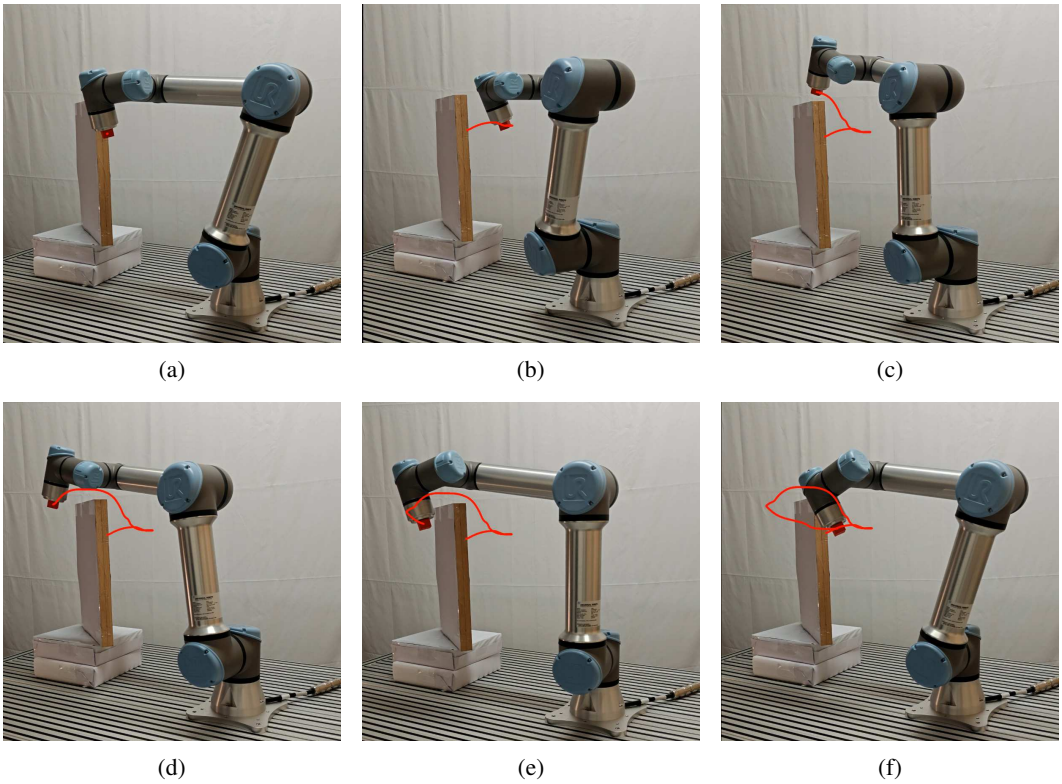

Figure 5: Snapshots of the physical obstacle-avoidance experiment.

positive modeled-link clearance in simulation, and effective path recovery. The method remains local and depends on obstacle-motion and geometric estimates; future work will address uncertainty-aware prediction, self-collision avoidance, and integration with global or learning-based planning.

REFERENCES

Martin Braquet and Efstathios Bakolas. Vector field-based collision avoidance for moving obstacles with time-varying elliptical shape. *IFAC-PapersOnLine*, 55(37):587–592, 2022.

Joseph Cenerini, Mohamed W Mehrez, Jeong-woo Han, Soo Jeon, and William Melek. Model predictive path following control without terminal constraints for holonomic mobile robots. *Control Engineering Practice*, 132:105406, 2023.

Bingjie Chen, Yancong Wei, Rihao Liu, Chenxi Han, Houde Liu, Chongkun Xia, Liang Han, and Bin Liang. Safe expeditious whole-body control of mobile manipulators for collision avoidance. *Biomimetic Intelligence and Robotics*, pp. 100301, 2026.

Moritz Eckhoff, Dennis Knobbe, Henning Zwirnmann, Abdalla Swikir, and Sami Haddadin. Towards connecting control to perception: High-performance whole-body collision avoidance using control-compatible obstacles. In *2023 IEEE/RSJ International Conference on Intelligent Robots and Systems (IROS)*, pp. 2354–2361. IEEE, 2023.

Lukas Huber, Jean-Jacques Slotine, and Aude Billard. Avoidance of concave obstacles through rotation of nonlinear dynamics. *IEEE Transactions on Robotics*, 40:1983–2002, 2023.

Yuri A Kapitanyuk, Anton V Proskurnikov, and Ming Cao. A guiding vector-field algorithm for path-following control of nonholonomic mobile robots. *IEEE Transactions on Control Systems Technology*, 26(4):1372–1385, 2017.

Leonidas Koutras, Konstantinos Vlachos, George S Kanakis, Fotios Dimeas, Zoe Doulgeri, and George A Rovithakis. Enforcing constraints for dynamic obstacle avoidance by compliant robots. In *2023 IEEE International Conference on Robotics and Automation (ICRA)*, pp. 5221–5227. IEEE, 2023.

Maximilian Krämer, Christoph Rösmann, Frank Hoffmann, and Torsten Bertram. Model predictive control of a collaborative manipulator considering dynamic obstacles. *Optimal Control Applications and Methods*, 41(4):1211–1232, 2020.

Shiqi Li, Ke Han, Xiao Li, Shuai Zhang, Youjun Xiong, and Zheng Xie. Hybrid trajectory replanning-based dynamic obstacle avoidance for physical human-robot interaction. *Journal of Intelligent & Robotic Systems*, 103(3):41, 2021.

Yiming Li, Xuemin Chi, Amirreza Razmjoo, and Sylvain Calinon. Configuration space distance fields for manipulation planning. *arXiv preprint arXiv:2406.01137*, 2024a.

Yiming Li, Yan Zhang, Amirreza Razmjoo, and Sylvain Calinon. Representing robot geometry as distance fields: Applications to whole-body manipulation. In *2024 IEEE International Conference on Robotics and Automation (ICRA)*, pp. 15351–15357. IEEE, 2024b.

Jie Liu, Hwa Jen Yap, and Anis Salwa Mohd Khairuddin. Review on motion planning of robotic manipulator in dynamic environments. *Journal of Sensors*, 2024(1):5969512, 2024.

Jinhao Liu, Jun Yang, Jianliang Mao, Tianqi Zhu, Qihang Xie, Yimeng Li, Xiangyu Wang, and Shihua Li. Flexible active safety motion control for robotic obstacle avoidance: A cbf-guided mpc approach. *IEEE Robotics and Automation Letters*, 10(3):2686–2693, 2025.

Charalampos Loukas, Momchil Vasilev, Rastislav Zimmerman, Randika KW Vithanage, Ehsan Mohseni, Charles N MacLeod, David Lines, Stephen Gareth Pierce, Stewart Williams, Jialuo Ding, et al. Transforming industrial manipulators via kinesthetic guidance for automated inspection of complex geometries. *Sensors*, 23(7):3757, 2023.

Jonathan Michaux, Patrick Holmes, Bohao Zhang, Che Chen, Baiyue Wang, Shrey Sahgal, Tiancheng Zhang, Sidhartha Dey, Shreyas Kousik, and Ram Vasudevan. Can not touch this: Real-time, safe motion planning and control for manipulators under uncertainty. *IEEE Transactions on Robotics*, 41:4719–4740, 2025.

Ken-Joel Simmoteit, Philipp Schillinger, and Leonel Rozo. Diffeomorphic obstacle avoidance for contractive dynamical systems via implicit representations. *arXiv preprint arXiv:2504.18860*, 2025.

Avantsa VSS Somasundar and G Yedukondalu. Six dof robot: inverse kinematics solution to path planning for intersecting pipes for welding operation and inverse jacobian comparison. *International Journal on Interactive Design and Manufacturing (IJIDeM)*, 18(5):3313–3322, 2024.

Balakumar Sundaralingam, Siva Kumar Sastry Hari, Adam Fishman, Caelan Garrett, Karl Van Wyk, Valts Blukis, Alexander Millane, Helen Oleynikova, Ankur Handa, Fabio Ramos, et al. Curobo: Parallelized collision-free robot motion generation. In *2023 IEEE International Conference on Robotics and Automation (ICRA)*, pp. 8112–8119. IEEE, 2023.

Mehran Ghafarian Tamizi, Marjan Yaghoubi, and Homayoun Najjaran. A review of recent trend in motion planning of industrial robots: Mg tamizi et al. *International Journal of Intelligent Robotics and Applications*, 7(2):253–274, 2023.

Julen Urain, Anqi Li, Puze Liu, Carlo D'Eramo, and Jan Peters. Composable energy policies for reactive motion generation and reinforcement learning. *The International Journal of Robotics Research*, 42(10):827–858, 2023.

Yalun Wen and Prabhakar R Pagilla. A novel 3d path following control framework for robots performing surface finishing tasks. *Mechatronics*, 76:102540, 2021.

Weijia Yao. Guiding vector fields for following occluded paths. In *Guiding Vector Fields for Robot Motion Control*, pp. 123–157. Springer, 2023a.

Weijia Yao. Path following control in 3d using a vector field. In *Guiding Vector Fields for Robot Motion Control*, pp. 39–62. Springer, 2023b.

Weijia Yao, Bohuan Lin, and Ming Cao. Integrated path following and collision avoidance using a composite vector field. In *2019 IEEE 58th Conference on Decision and Control (CDC)*, pp. 250–255. IEEE, 2019.

Weijia Yao, Héctor Garcia de Marina, Bohuan Lin, and Ming Cao. Singularity-free guiding vector field for robot navigation. *IEEE Transactions on Robotics*, 37(4):1206–1221, 2021.

Yu Zhou, Jesús Bautista, Weijia Yao, and Héctor García De Marina. Inverse kinematics on guiding vector fields for robot path following. In *2025 IEEE International Conference on Robotics and Automation (ICRA)*, pp. 8635–8641. IEEE, 2025.

Tianqi Zhu, Jianliang Mao, Linyan Han, Chuanlin Zhang, and Jun Yang. Real-time dynamic obstacle avoidance for robot manipulators based on cascaded nonlinear mpc with artificial potential field. *IEEE Transactions on Industrial Electronics*, 71(7):7424–7434, 2023.

AI USE STATEMENT

Generative AI tools were used to assist with language polishing, formatting checks, drafting and revising portions of the manuscript, including parts of the Introduction, and localized modifications to portions of the experimental code. The research methodology, experimental design, analysis, and conclusions were developed by the authors. All AI-assisted text and code modifications were reviewed and verified by the authors.